11th International Symposium on Turbulence and Shear Flow Phenomena (TSFP11)
Southampton, UK, July 30 to August 2, 2019

EFFECT OF TRANSVERSE CURVATURE ON TURBULENT CONCENTRIC ANNULAR PIPE FLOW AND STRUCTURES

Edris Bagheri
Department of Mechanical Engineering
University of Manitoba, Winnipeg, MB, R3T 5V6, Canada
bagherie@myumanitoba.ca

Bing-Chen Wang
Department of Mechanical Engineering
University of Manitoba, Winnipeg, MB, R3T 5V6, Canada
Bingchen.Wang@umanitoba.ca

ABSTRACT

The effects of surface curvature on fully-developed turbulent concentric annular pipe flow and structures have been studied using direct numerical simulations (DNS). A comparative study based on four radius ratios of a concentric pipe (for $R_i/R_o = 0.1$–0.7) are compared at Reynolds number $Re_{D_h} = 8900$. Here, R_i and R_o are the radii of the inner and outer pipes, respectively, and D_h is the hydraulic diameter. The sufficiency of the computational domain is investigated by comparing the results of premultiplied energy spectra and two-point correlation coefficients. Coherent flow structures near the inner and outer walls are investigated in both physical and spectral spaces. The interaction between the inner and outer boundary layers is studied based on analysis of Reynolds shear stresses. The dynamics of streamwise-elongated counter-rotating Taylor-Görtler (TG) vortices are also investigated. In the outer layer of turbulent annular flow, very large-scale motions (VLSMS) are observed, which appear as a chain of hairpin structures.

1 INTRODUCTION

Turbulent flow confined within a concentric pipe is an interesting subject, which has important engineering applications to, e.g. double pipe heat-exchangers and the air bypass over the combustion chamber of a jet engine. Owing to the difference in the surface curvature of the inner and outer pipes, the spatial and temporal scales of turbulence are different near these two walls of a concentric pipe. The interaction between these two boundary layers results in an asymmetric mean velocity profile, which makes the flow physics more complex than that of a round pipe or plane channel flow.

In his pioneering study, Rayleigh (1917) conducted a theoretical analysis of the instability of an inviscid fluid over a concave wall. Later, Görtler (1954) extended the analysis to viscous fluids and indicated that the flow instability can lead to counter-rotating vortex pairs aligned in the mean flow direction, which are now referred to as Taylor-Görtler (TG) vortices. These vortex pairs were later observed in the wind tunnel experimental study of Gregory & Walker (1956). Wilcken (1930) measured velocity profiles by using a Pitot tube in a water channel to study the effects of curvature on the turbulent flow field. They showed that variation in the first-order flow statistics was much larger than the prediction of the turbulence mixing length model. So & Mellor (1973) performed a wind-tunnel experiment to study the boundary layer along a convex surface. They observed a reverse relationship between the surface curvature and Reynolds stresses along the convex wall. Neves *et al.* (1994) used DNS to study the effects of the convex wall on the development of a turbulent boundary layer. They observed that as the curvature increases, the skin friction increases, associated with a reduction of the log-law region and turbulent intensities.

Closely related to the studies of flow over a single concave or convex surface reviewed above, there are several investigations into turbulent flow in concentric or eccentric annular pipes. Nouri *et al.* (1993) conducted extensive experimental studies on turbulent flows in concentric and eccentric annular pipes using laser Doppler velocimetry (LDV) for Newtonian and Non-Newtonian fluids at $Re_{D_h} = 8900$ (based on D_h and bulk mean velocity U_m). They showed the effect of eccentricity on the characteristics of the flow field. Chung *et al.* (2002) performed a DNS study of turbulent concentric annular flow at $Re_{D_h} = 8900$, identical to the experimental conditions of Nouri *et al.* (1993). They examined the effect of transverse curvature on turbulent statistics by comparing the results of two radius ratios of $R_i/R_o = 0.1$ and 0.5. Recently, Ghaemi *et al.* (2015) performed particle image velocimetry (PIV) measurements of a turbulent concentric annular pipe flow at very high Reynolds numbers ($Re_{D_h} = 59200$–90000). Their experimental data shows that the maximum mean velocity and the zero shear stress do not occur at the same radial position.

Thus far, a detailed study of the effects of transverse curvature on the turbulent flow in a concentric annular pipe is still lacking in the current literature. In view of this, we aim at conducting a systematic DNS study based on various radius ratios ($R_i/R_o = 0.1$–0.7). The effects of transverse curvature and the interaction of the inner and outer bound-

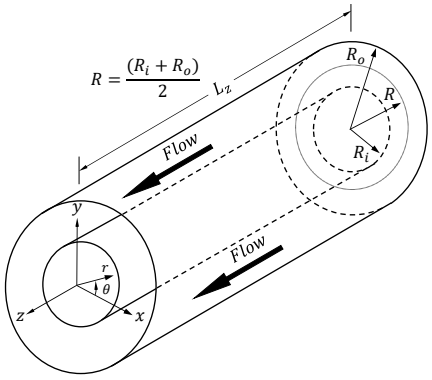

Figure 1: Computational domain and coordinates.

ary layers are scrutinized through a comparative study. Coherent flow structures are identified in both physical and spectral spaces, and their scales near the inner and outer walls are investigated.

The remainder of this paper is organized as follows: in section 2, the numerical algorithm for solving the governing equations are introduced, and four test cases (of different radius ratios) are described, in section 3.1 the sufficiency of the computational domain is investigated. In section 3.2, the flow physics and statistical moments of the turbulence field are analyzed, including the mean velocities and Reynolds stresses. In section 3.3, the coherent flow structures are examined in both physical and spectral spaces. Finally, in section 4, major findings of this research are summarized.

2 ALGORITHM AND TEST CASES

The equations that govern an incompressible flow with respect to a cylindrical coordinate system read

$$\nabla \cdot \vec{u} = 0, \tag{1}$$

$$\frac{\partial \vec{u}}{\partial t} + \vec{u} \cdot \nabla \vec{u} = -\frac{1}{\rho}\nabla p + \nu \nabla^2 \vec{u} - \frac{\Pi}{\rho}\hat{\mathbf{e}}_z, \tag{2}$$

where p, ρ and ν denote pressure, density and kinematic viscosity, respectively. Π is the constant mean axial pressure gradient that drives the flow, and $\hat{\mathbf{e}}_z$ is the base unit vector of the z-direction, with $|\hat{\mathbf{e}}_z| \equiv 1$.

An in-house computer code based on the pseudo-spectral method has been used for performing DNS, which was developed using the FORTRAN 90/95 programming language. Message passing interface (MPI) libraries are employed to parallelize the computing processes. For domain discretization, equally-spaced grid points are used in both the streamwise and azimuthal directions, and Chebyshev-Gause-Lobatto points are used in the radial direction for a better spatial resolution near the walls. To expand the velocity and pressure fields, Fourier series are applied to the streamwise and azimuthal directions, and the Lagrange polynomials are used in the wall-normal direction. Aliasing errors are removed by using the 3/2 rule. The time splitting method developed by Karniadakis *et al.* (1991) with a third-order temporal accuracy is used for the time integration. Periodic boundary conditions are applied in the streamwise and azimuthal directions, and no-slip boundary conditions are imposed on all solid surfaces. All computations were performed on the WestGrid (Western Canada Research Grid) supercomputers. Figure 1 shows a schematic diagram of the computational domain and coordinate system of the turbulent concentric annular pipe flow under testing. Here, z, r, and θ denote the axial (streamwise), radial and azimuthal coordinates, respectively, and u_z, u_θ and u_r represent velocity components in the corresponding directions. The radius of the cylindrical channel center is $R = (R_i + R_o)/2$. A summary of test cases and grid resolutions is given in Table 1. Four radius ratios (for $R_i/R_o = 0.1, 0.3, 0.5$ and 0.7) are compared at a fixed Reynolds number of $Re_{D_h} = 8900$. In order to maintain the accuracy required by DNS, the grid resolution is kept at $\Delta_z^+ \leq 14.3$ and $\Delta_\theta^+ \leq 7.71$ in the streamwise and azimuthal directions, respectively. The radial resolution is kept at $\Delta_r^+ \leq 0.15$ near the walls and $\Delta_r^+ \leq 12.96$ in the central domain. Here, superscript "+" denotes a quantity expressed in the wall coordinate (through non-dimensionalization based on ν and u_τ).

Table 1: Summary of test cases.

R_i/R_o	$N_z \times N_\theta \times N_r$	$L_z \times L_\theta \times L_r$
0.1	$392 \times 256 \times 64$	$12\pi\delta \times 2\pi \times 2\delta$
0.3	$392 \times 240 \times 64$	$12\pi\delta \times 3\pi/2 \times 2\delta$
0.5	$392 \times 196 \times 64$	$12\pi\delta \times 3\pi/4 \times 2\delta$
0.7	$392 \times 144 \times 64$	$12\pi\delta \times \pi/2 \times 2\delta$

3 RESULT ANALYSIS

3.1 Minimal pipe lenght

The choice of computational domain size is crucial for obtaining an accurate solution of the turbulent flow field. The accuracy of the predicted flow field depends on the numerical algorithm, boundary conditions and computational domain size. A highly accurate algorithm by itself is not sufficient to warrant a correct prediction of the principal flow physics associated with the most energetic eddy motions. If the computational domain is overly small, energetic eddies will not be captured by DNS, which necessarily leads to an artificial distortion or chopping off of the energy spectra at low wavenumbers. The sufficiency of a computational domain sized can be investigated in both physical and spectral spaces based on the criteria of two-point correlation and premultiplied energy spectra.

Figure 2 compares the two-point correlation coefficients of the different cases in the streamwise direction. The two-point correlations are calculated at $r^+ = 15$, where the maximum of turbulence intensity occurs. Figure 2 shows that R_{zz} marginally goes to zero for $z/\delta \geq 6$ in all cases, which indicates sufficiency of the streamwise computational domain size. It is worth mentioning that the choice of domain size based on two-point correlation in the physical space may not be conclusive, and it is necessary to study the energy spectra of the flow field in the spectral space to ensure that those energetic eddies of low wavenumbers are fully captured. The premultiplied energy spectra in the streamwise direction is defined as:

$$\phi_{ii}(\lambda_z, r) = k_z \langle \hat{u}_i(\lambda_z, r) \hat{u}_i^*(\lambda_z, r) \rangle, \tag{3}$$

where k_z and λ_z are the wavenumber and wavelength of the streamwise direction, respectively, and $\langle \cdot \rangle$ denotes spatial and temporal averaging. Fourier transform of the velocity vectors is denoted by $\hat{u}_i$, and $\hat{u}_i^*$ denotes its conjugate. Figure 3 shows the premultiplied energy spectra as a function of the non-dimensionalized wavelength in the global

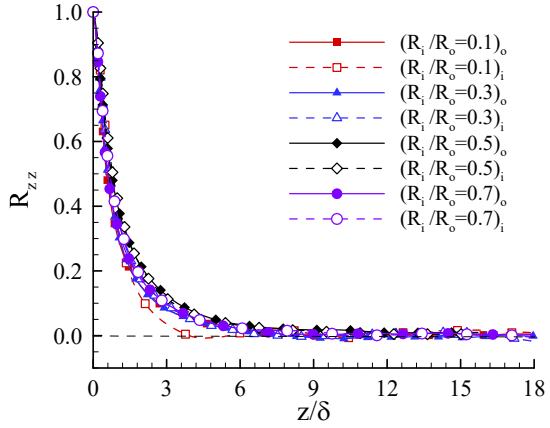

Figure 2: Two-point correlation coefficient at $r^+ = 15$.

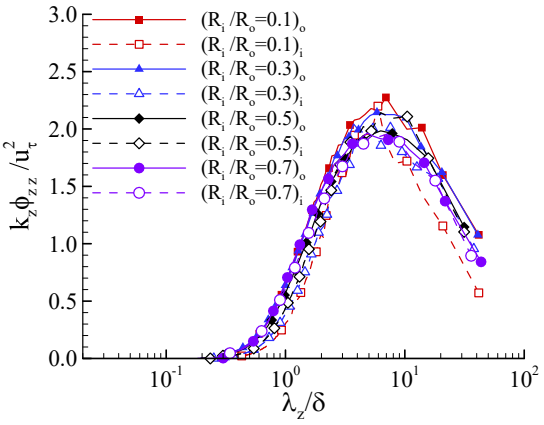

Figure 3: One-dimensional energy spectra at $r^+ = 15$.

coordinate ($\lambda_z/\delta = 2\pi/k_z\delta$, where δ is one half the pipe gap). Clearly, the streamwise computational domain size $L_z = 12\pi\delta$ used in the current DNS is large enough to capture most of the turbulence kinetic energy (TKE) such that the TKE at the lowest wavenumber (k_1) near the outer wall is only 25% of the peak value in the case of $R_i/R_o = 0.1$.

3.2 Flow statistics

The mean flow parameters are given in Table 2. In the table, $Re_\tau = \delta_t u_\tau/\nu$, which is defined based on the wall friction velocity u_τ and boundary layer thickness δ_t. The boundary layer thickness, δ_t, is the distance across a boundary layer from the wall to the point where the streamwise mean velocity is maximum (or alternatively, the Reynolds shear stress is zero). From Table 2, it is evident that the skin friction coefficient ($C_f = \tau_w/\frac{1}{2}\rho U_m^2$) increases with an increasing curvature (or, with a decreasing value of radius ratio R_i/R_o). Here, U_m is the bulk mean velocity and τ_w is the averaged wall shear stress over the inner or outer walls.

The law of the wall can be derived by postulating a length scale $\ell = \kappa_\theta r$. Here, κ_θ is the Kármán constant, which shows the ratio of the outer length scale to the viscous length scale (Adrian, 2007). The law of the wall in the log-law region can be stated as:

$$\langle u_z\rangle^+ = \langle u_z\rangle/u_\tau = \frac{1}{\kappa_\theta} ln(r^+) + \beta_\theta. \qquad (4)$$

Direct numerical simulation enables us to accurately measure these two quantities κ_θ and β_θ. The Kármán constant

Table 2: Mean flow parameters.

R_i/R_o	0.1	0.3	0.5	0.7
Re_{D_h}	8900	8900	8900	8900
Re_{τ_i}	196	177	164	159
Re_{τ_o}	105	117	125	131
C_{f_i}	0.0132	0.0102	0.0093	0.0092
C_{f_o}	0.0085	0.0086	0.0088	0.0090

is obtained from the following equation:

$$\frac{1}{\kappa_\theta} = r^+ \frac{\partial\langle u_z\rangle^+}{\partial r^+}. \qquad (5)$$

Substituting Eq. (5) into Eq. (4) β_θ to obtain:

$$\beta_\theta = \langle u_z\rangle^+ - r^+ \frac{\partial\langle u_z\rangle^+}{\partial r^+} ln(r^+). \qquad (6)$$

Figures 4a and 4b show the values of the two constants κ_θ and β_θ of the logarithmic law of the wall for all cases. Clearly, as the radius ratio decreases, the plateau region reduces, especially near the inner wall. Figure 4b shows the value of the additive constant β_θ on the inner and outer wall sides for all test cases. Figure 5a contrasts the streamwise mean velocity profiles of the inner and outer walls for the case of $R_i/R_o = 0.1$. The various regions and layers for describing the near-wall flow are distinguished for the outer wall. The velocity profiles of both the inner and outer walls strictly follow the linear law of the wall for the viscous sublayer. The log-law region is developed over a wider extended range for the outer wall than for the inner wall, which is consistent with a greater plateau region of the outer wall shown in figure 4a. Figure 5b compares the mean velocity profiles of all cases with respect to the global coordinate. The boundary layer evolving over the outer wall is thicker than that over the inner wall. Consequently, the velocity on the inner side is higher than that on the outer side. The characteristics of the turbulent boundary layer near the inner wall with higher velocities are similar to those of an accelerating boundary layer. Furthermore, it is observed that the wake region on the inner side is diminished, which is consistent with the experimental observation of Bourassa & Thomas (2009) based on their oil-film interferometry measurement of a highly accelerated turbulent boundary layer.

Figure 6 compares the profiles of the Reynolds normal stresses of four test cases for both the inner and outer walls. The Reynolds normal stresses are scaled based on the local friction velocities of the inner and outer walls accordingly. From figure 6, the transverse curvature effects can be readily identified by comparing the results of the inner and outer walls of each case. The position of the peak is consistent near the inner and outer sides in all cases and occurs at $r^+ = 15$. Here, the wall coordinate is defined as $r^+ = (r - R_i)u_{\tau i}/\nu$ and $r^+ = (R_o - r)u_{\tau o}/\nu$ for the inner and outer walls, respectively. The magnitude of turbulence intensity associated with the streamwise velocity fluctuations is the highest, followed by azimuthal and radial components. The difference between the inner and outer walls becomes more apparent as the radius ratio decreases. It is worth noting that the radial and azimuthal components of turbulence intensity are more sensitive to the transverse curvature than does the axial component.

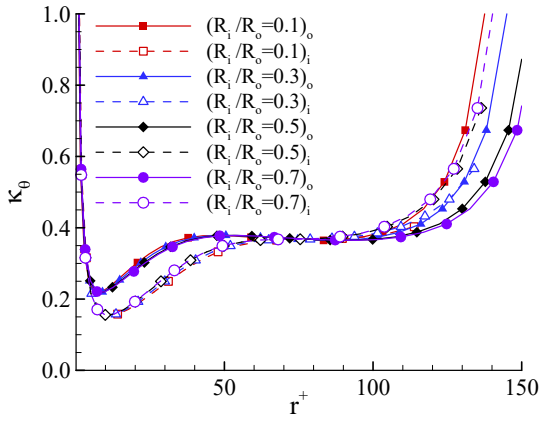

(a) Profile of κ_θ for the mean axial velocity

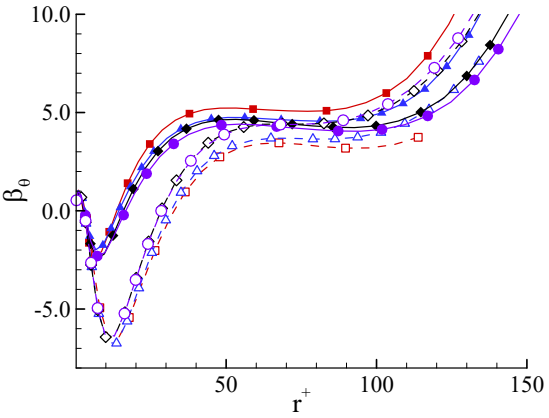

(b) Profile of β_θ of the mean axial velocity

Figure 4: Values of constants κ_θ and β_θ of the log-law of the wall associated with the mean axial flow in a concentric annular pipe.

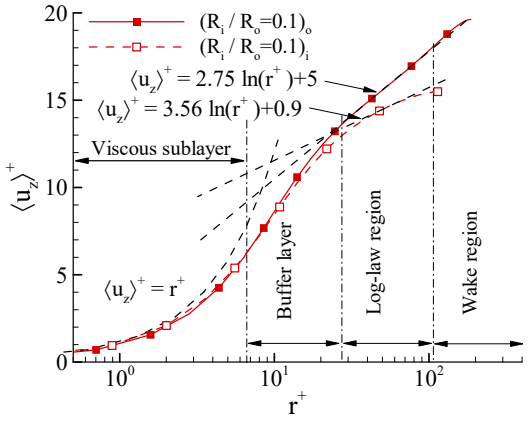

(a) Displayed in the wall coordinate

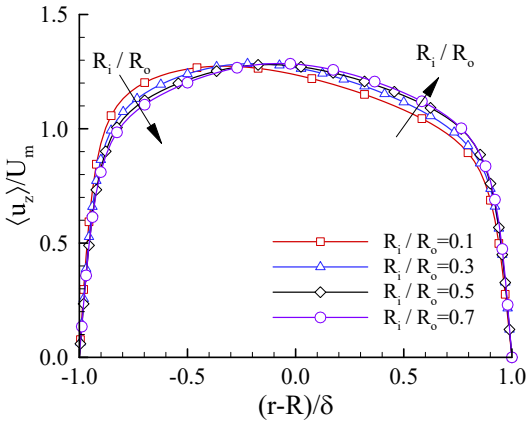

(b) Displayed in the global coordinate

Figure 5: Profile of the non-dimensionalzed mean axial velocity displayed with respect to the wall and global coordinates.

The study of the Reynolds shear stress is the key to better understand the interaction between the inner and outer boundary layers. Figure 7 compares the Reynolds shear stresses of all test cases with respect to the global coordinates. As is evident in the figure, the magnitude of the Reynolds shear stresses is higher on the outer wall side than on the inner wall side. Apparently, as shown in the figure, the difference between the two sides of the concentric annular pipe becomes more pronounced as the radius ratio decreases. The boundary layer thickness (δ_t) can be measured by finding the point where Reynolds shear stresses cross the zero. Through a shear stress balance, it can be shown that this difference in the Reynolds shear stresses between the outer and inner walls further results in differences in the wall friction velocities and boundary-layer thicknesses on the two sides of the concentric annular pipe.

3.3 Turbulent flow structures

From the above analysis, it is understood that a decrease of the radius ratio results in a bigger discrepancy in the magnitudes of Reynolds stresses between the inner and outer walls. It would be interesting to further understand the effect of the radius ratio on the dynamics of turbulent flow structures within the inner and outer boundary layers. The scale of energetic turbulent flow structures is identified using the streamwise velocity spectrum and visualized using the iso-surfaces of the swirling strength (λ_{ci}).

The spectrum map shows the premultiplied energy spectra as a function of wavelength (λ_z) and wall-normal distance (r^+), which vividly demonstrates the energy-containing scales of near-wall turbulence. In order to show the curvature effects, two cases of the smallest and largest radius ratios (i.e., $R_i/R_o = 0.1$ and 0.7) are directly contrasted in our study. Figure 8 compares the contours of the one-dimensional (1D) premultiplied energy spectra of the streamwise velocity fluctuations of the inner and outer walls. The spectrum maps show three regions of high-, intermediate- and low-intensity cores. The borders of these three regions correspond $0.875\max(\phi_{zz})$, $0.625\max(\phi_{zz})$ and $0.375\max(\phi_{zz})$. The border that separates the spectrum maps of the inner and outer walls is shown with a dashed black line. The near-wall streaks are the most energetic structures in the turbulent flow field. From figure 8, it is clear that the peak value of the premultiplied energy spectrum corresponding to the most energetic flow structures occurs at $r^+ \approx 15$ near the inner and outer walls for both cases. The streamwise wavelength corresponding to the energetic flow structures for the case of $R_i/R_o = 0.7$ is $\lambda_z^+ \approx 1000$ on both the inner and outer sides. However, for the case of $R_i/R_o = 0.1$, those wavelengths are $\lambda_z^+ \approx 1100$ and $\lambda_z^+ \approx 900$ for the inner and outer walls, respectively. This asymmetrical radial distribution of the premultiplied energy spectrum is a consequence of the curvature difference between the inner and outer walls. This also

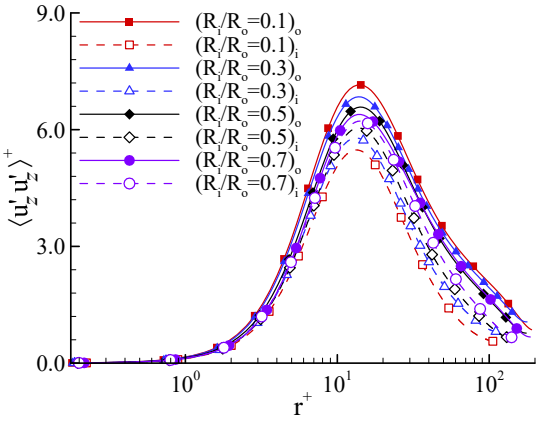

(a) axial component

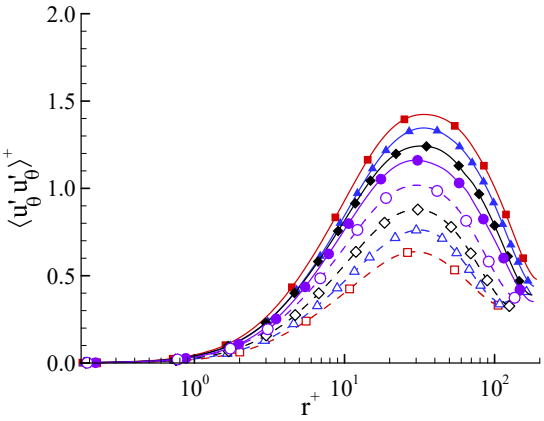

(b) azimuthal component

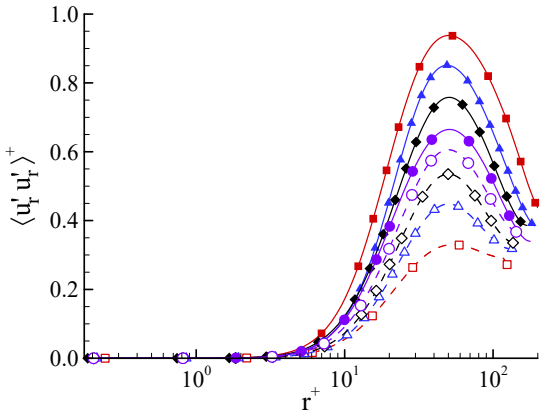

(c) radial component

Figure 6: Profiles of Reynolds normal stresses at various radius ratios.

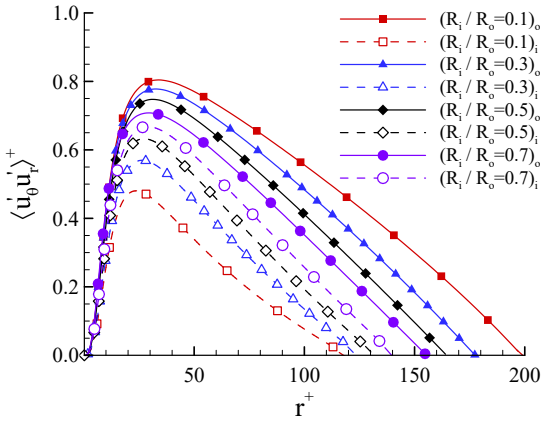

Figure 7: Profiles of Reynolds shear stresses at various radius ratios.

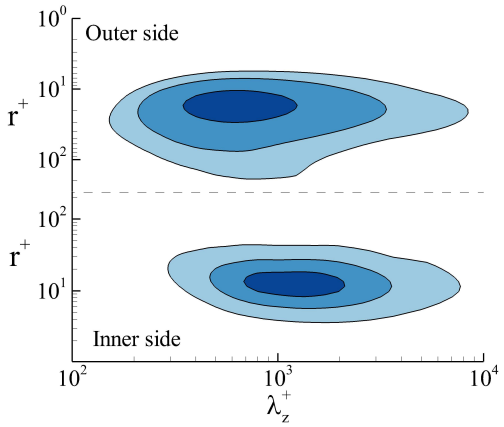

(a) $k_z\phi_{zz}/u_\tau^2$ for the case of $R_i/R_o = 0.1$

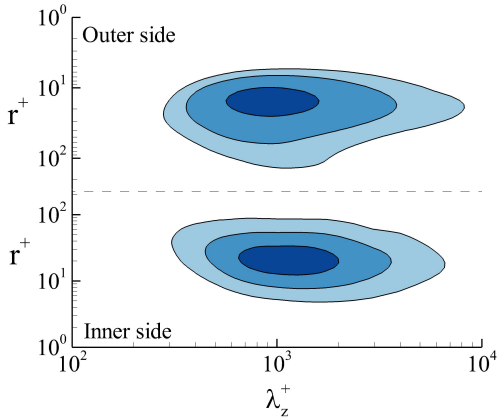

(b) $k_z\phi_{zz}/u_\tau^2$ for the case of $R_i/R_o = 0.7$

Figure 8: Contours of premultiplied one-dimensional streamwise spectral energy density $k_z\phi_{zz}(\lambda_z, r^+)$ for cases of $R_i/R_o = 0.1$ and $R_i/R_o = 0.7$. Three regions of different energy levels are distinguished using isopleths, corresponding to $0.875\max(\phi_{zz}), 0.625\max(\phi_{zz})$ and $0.375\max(\phi_{zz})$, respectively.

clearly indicates that as the curvature increases, the near-wall streaks become increasingly elongated near the inner wall and shortened near the outer wall.

Figure 9 shows the iso-surfaces of the swirling strength ($\lambda_{ci} = 1.0$) for the case of radius ratio $R_i/R_o = 0.5$. Only one-half of the streamwise and a quarter of the cross-sectional domain is plotted to improve the visual effects. The presence of large-scale motions in the form of hairpin packets in the logarithmic region is evident. The TG vortices are visualized in figure 10 using the contours of $\overline{\omega_z'}^+$ and velocity vectors in the cross-stream plane for the case $R_i/R_o = 0.1$. Here, $\omega_z' = \frac{1}{r}\frac{\partial r u_\theta'}{\partial r} - \frac{1}{r}\frac{\partial u_r'}{\partial \theta}$, which is the fluctuating streamwise vorticity, and an overbar denotes averaging over time and over the homogeneous streamwise direction. The method of visualization used here follows that of Yang & Wang (2018) who studied TG-like vortices in

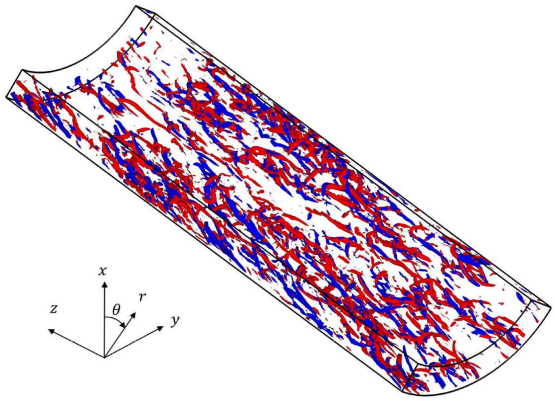

Figure 9: Contour of iso-surface of swirling strength of $\lambda_{ci} = 1.0$ on the concave wall side

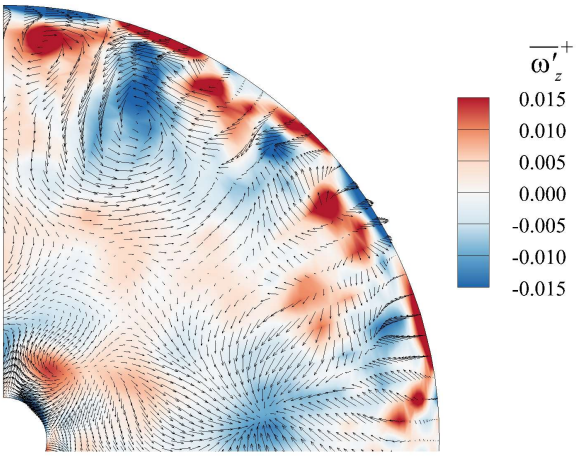

Figure 10: Contours of fluctuating streamwise vorticity $\overline{\omega'_z}^+$ superimposed with velocity vectors composed of $\overline{u'_\theta}$ and $\overline{u'_r}$, averaged over time and over the homogenouse streamwise direction of the domain.

a streamwise rotating channel flow using DNS. Only one-quarter of the cross-section is shown to ensure a clear view of the velocity field. Clearly, owing to the curvature difference between the concave and convex walls, the TG vortices are mostly concentrated near the outer wall.

4 Conclusion

DNS of turbulent flow in a concentric annular pipe flow has been performed to investigate the effect of transverse curvature on turbulent flow statistics and structures. The comparative study includes four test cases of different radius ratio for $R_i/R_o = 0.1, 0.3, 0.5$ and 0.7. It is found that the logarithmic law of the wall does not hold firmly as the transverse curvature increases. The turbulence intensities are larger near the outer wall than near the inner wall. The study of the Reynolds shear stress with respect to the global coordinates shows that boundary layer is thicker near the outer wall than near the inner wall. The difference in the boundary-layer thickness becomes more apparent as the curvature ratio decreases. Study of one-dimensional energy spectra shows the effect of transverse curvature on the characteristic scale of energetic turbulent flow structures. It is found that the transverse curvature causes the streamwise scale of turbulent flow structures to increase near the inner wall but reduce near the outer wall. By use of time-averaged contour of streamwise fluctuating vorticity $\overline{\omega'_z}^+$ and swirling strength λ_{ci}, very long streamwise elongated counter-rotating TG vortex pairs are observed. Owing to the curvature difference between the concave and convex walls, the TG vortices are mostly concentrated near the outer wall of the concentric annular pipe.

REFERENCES

Adrian, R. J. 2007 Hairpin vortex organization in wall turbulence. *Phys. Fluids* **19** (4), 041301.

Bourassa, C. & Thomas, F. O. 2009 An experimental investigation of a highly accelerated turbulent boundary layer. *J. Fluid Mech.* **634**, 359–404.

Chung, S. Y., Rhee, G. H. & Sung, H. J. 2002 Direct numerical simulation of turbulent concentric annular pipe flow, part 1: Flow field. *Int. J. Heat Mass Transfer* **23** (4), 426–440.

Ghaemi, S., Rafati, S., Bizhani, M. & Kuru, E. 2015 Turbulent structure at the midsection of an annular flow. *Phys. Fluids* **27** (10), 105102.

Görtler, H. 1954 On the three-dimensional instability of laminar boundary layers on concave walls. *NACA TM-137* .

Gregory, N. T. & Walker, W. S. 1956 *The effect on transition of isolated surface excrescences in the boundary layer*. HM Stationery Office.

Karniadakis, G. E., Israeli, M. & Orszag, S. A. 1991 High-order splitting methods for the incompressible Navier-Stokes equations. *J. Comp. Phys.* **97** (2), 414–443.

Neves, J. C., Moin, P. & Moser, R. D. 1994 Effects of convex transverse curvature on wall-bounded turbulence. part 1. the velocity and vorticity. *J. Fluid Mech.* **272**, 349–382.

Nouri, J. M., Umur, H. & Whitelaw, J. H. 1993 Flow of newtonian and non-newtonian fluids in concentric and eccentric annuli. *J. Fluid Mech.* **253**, 617–641.

Rayleigh, L. 1917 On the dynamics of revolving fluids. *Proc. R. Soc. London* **93** (648), 148–154.

So, R. M. & Mellor, G. L. 1973 Experiment on convex curvature effects in turbulent boundary layers. *J. Fluid Mech.* **60** (1), 43–62.

Wilcken, H. 1930 Effect of curved surfaces on turbulent boundary layers. *NASA TTF* **11421**.

Yang, Z. & Wang, B.-C. 2018 Capturing Taylor–Görtler vortices in a streamwise-rotating channel at very high rotation numbers. *J. Fluid Mech.* **838**, 658–689.